In situ high-temperature EBSD and 3D phase field studies of the austenite-ferrite transformation in a medium Mn steel

Farahani, Hussein; Zijlstra, Gerrit; Mecozzi, Maria Giuseppina; Ocelík, Václav; De Hosson, Jeff Th M.; Van Der Zwaag, Sybrand

DOI
10.1017/S143192761900031X

Publication date
2019

Document Version
Final published version

Published in
Microscopy and Microanalysis

Citation (APA)
Farahani, H., Zijlstra, G., Mecozzi, M. G., Ocelík, V., De Hosson, J. T. M., & Van Der Zwaag, S. (2019). In situ high-temperature EBSD and 3D phase field studies of the austenite-ferrite transformation in a medium Mn steel. *Microscopy and Microanalysis*, *25*(3), 639-655. https://doi.org/10.1017/S143192761900031X

Microscopy and Microanalysis (2019), **25**, 639–655
doi:10.1017/S143192761900031X

Microscopy AND Microanalysis

Original Article

In Situ High-Temperature EBSD and 3D Phase Field Studies of the Austenite–Ferrite Transformation in a Medium Mn Steel

Hussein Farahani[1,2]*, Gerrit Zijlstra[3], Maria Giuseppina Mecozzi[2], Václav Ocelík[3], Jeff Th. M. De Hosson[3] and Sybrand van der Zwaag[1,4]

[1]Novel Aerospace Materials group, Faculty of Aerospace Engineering, Delft University of Technology, 2629 HS Delft, The Netherlands; [2]Department of Materials Science and Engineering, Delft University of Technology, 2628 CD Delft, The Netherlands; [3]Department of Applied Physics, Materials Innovation Institute and Zernike Institute for Advanced Materials, University of Groningen, 9747 AG Groningen, The Netherlands and [4]School of Materials Science and Engineering, Tsinghua University, Beijing, China

Abstract

In this research, *in situ* high-temperature electron backscattered diffraction (EBSD) mapping is applied to record and analyze the migration of the α/γ interfaces during cyclic austenite–ferrite phase transformations in a medium manganese steel. The experimental study is supplemented with related 3D phase field (PF) simulations to better understand the 2D EBSD observations in the context of the 3D transformation events taking place below the surface. The *in situ* EBSD observations and PF simulations show an overall transformation behavior qualitatively similar to that measured in dilatometry. The behavior and kinetics of individual austenite–ferrite interfaces during the transformation is found to have a wide scatter around the average interface behavior deduced on the basis of the dilatometric measurements. The trajectories of selected characteristic interfaces are analyzed in detail and yield insight into the effect of local conditions in the vicinity of interfaces on their motion, as well as the misguiding effects of 2D observations of processes taking place in 3D.

Key words: austenite–ferrite interface migration, cyclic partial phase transformations, EBSD, medium manganese steel, phase field simulation, steel

(Received 7 September 2018; revised 15 January 2019; accepted 22 February 2019)

Introduction

The science of solid-state phase transformation in crystalline materials in general and in steels in particular has been a stimulating field of research for decades. The transformations of interest take place via migration of interfaces over relatively large distances at the micrometer scale and play a key role in the formation of transient and final microstructures. As many mechanical and physical properties of a material depend on its microstructure, it is of great importance to understand the parameters controlling the migration behavior of the interfaces between the parent and product phases (Raghavan & Cohen, 1975; Kostorz, 2001; Christian, 2002; Gottstein, 2004).

In steels, the phase transformation from austenite (γ) to ferrite (α) and *vice versa* proceeds by migration of their interfaces (Purdy et al., 2011) and this migration behavior can be used to control the final mechanical properties (Ashby, 2013). Excluding local topology effects, the interface migration behavior depends on the dissimilarities in crystal structure between both phases and the average chemical composition of the alloy, but even more so the local chemical compositions at the interface and the transformation temperature (Purdy, 1978*a*, 1978*b*). Many models have been proposed to incorporate the effect of various parameters on the rate of interface migration during ferrous phase transformations, as nicely summarized in a comprehensive review paper (Gouné et al., 2015). In such models, the phase transformation is modeled by reducing the actual interface to a mathematical surface characterized with multiple variables and parameters such as the interface thickness (Svoboda et al., 2011), trans-interface diffusivity (Gamsjäger & Rettenmayr, 2015), interface energy (Militzer et al., 2014) and crystallographic orientation relationship (OR) between two crystals in contact (Ecob & Ralph, 1981). Yet, all these models explicitly or implicitly assume that the local interface movement is the same for each interface and does not vary along a particular interface, except near triple lines and quadrupole points. In the following we refer to triple junctions as being where three or more interfaces meet.

The actual motion of real α/γ interfaces has been studied experimentally with different *in situ* techniques such as optical microscopy (OM) (Watanabe et al., 2004; Witusiewicz et al., 2005, 2013), laser scanning confocal microscopy (Phelan et al., 2005; Chen et al., 2013*a*; Cheng et al., 2014; Sainis et al., 2018), scanning electron microscope (SEM)/electron backscattered diffraction (EBSD) (Prior et al., 2003; Seward et al., 2006; van der Zwaag et al., 2006; Fukino & Tsurekawa, 2008; Mishra & Kubic, 2008; Fukino et al., 2011; Torres & Ramírez, 2011; Enomoto & Wan, 2017; Shirazi et al., 2018) photoemission electron

---

*Author for correspondence: H. Farahani, E-mail: H.Farahani@tudelft.nl

Cite this article: Farahani H, Zijlstra G, Mecozzi MG, Ocelík V, De Hosson JTh M, van der Zwaag S (2019) *In Situ* High-Temperature EBSD and 3D Phase Field Studies of the Austenite–Ferrite Transformation in a Medium Mn Steel. *Microsc Microanal* **25**, 639–655. doi:10.1017/S143192761900031X

microscopy (Middleton & Form, 1975; Middleton & Edmonds, 1977; Edmonds & Honeycombe, 1978), and transmission electron microscopy (Brooks et al., 1979; Moine et al., 1985; Onink et al., 1995; Mompiou et al., 2015; Guan et al., 2017; Liu et al., 2017; Du et al., 2018). Each of these techniques has its own advantages and drawbacks in accurately documenting the interface motion as a function of the imposed external parameters (such as temperature and composition) and the transient local conditions (such as triple junctions where three or more boundaries meet, neighboring interfaces and grain boundaries and overall degree of transformation). Typical instrumental constraints are the spatial resolution, the imaging speed, the field of view, and finally the possibility to measure the crystal structure and orientation of the phases in contact at the interface.

With the recent advent of high-temperature (HT) EBSD techniques, *in situ* SEM/EBSD emerges as a potentially useful technique for *in situ* observation of the local dynamics during the microstructural evolution (Mishra, 2012). Its ability to determine the crystal structure and relative orientation of the growing and shrinking grains of the transient parent and product phases (Wright et al., 2005; Fukino & Tsurekawa, 2008; Nowell et al., 2009; Kobler et al., 2012; Zhang et al., 2016; Zijlstra et al., 2017) is a major advantage over the conventional HT (optical and electron) imaging techniques. Therefore, *in situ* EBSD can yield quasi-continuous information on the motion of individual α/γ interfaces during the phase transformation, facilitating full quantification of the evolution of the crystallographic texture. However, in this method, temperature control of the sample can be difficult and the data analysis needs to consider a possible intrusion of surface artifacts on the achieved results (Gourgues-Lorenzon, 2007; Wright et al., 2014). In general, the observed migration behavior of interfaces in 2D is strongly affected by the transformation behavior taking place just below the surface, i.e. it depends on the (truncated) 3D topology of the grains monitored on the free surface (Zhang et al., 2017). Hence, "medium-scale" 3D modeling approaches using micromechanics or phase field (PF) simulation are recommended to be coupled to EBSD results in order to get a more complete insight into the processes responsible for the observed features at 2D interfaces (Gourgues-Lorenzon, 2009).

The results of such *in situ* EBSD experiments also depend on the nature of the transformation experiment itself. In conventional heating and cooling experiments, the phase transformation phenomena to be observed are related to both nucleation and growth, each having their own features and requiring different measuring techniques. The recently introduced cyclic partial phase transformation (CPPT) approach (Chen & van der Zwaag, 2016) provides a simple method to exclude the nucleation effects such that all observations are related to grain growth (and shrinkage) only. In a CPPT route, the temperature is cycled in such a manner that the α and γ phases both are present at all times and the transformation proceeds via back-and-forth migration of existing α/γ interfaces. Apart from the expected forward and backward migration of the interfaces, the so-called "stagnant stages" have also been observed during which the $\alpha \rightarrow \gamma$ and $\gamma \rightarrow \alpha$ interface migration is halted while a clear overall thermodynamic driving force for further transformation is present. The temporary pinning of the α/γ interfaces is due to a build-up of enrichment in alloying elements, in particular Mn, in or near the migrating α/γ interfaces (Chen et al., 2011; Chen & van der Zwaag, 2012a, 2012b; Chen, 2013; Zhu et al., 2017).

In the present work, *in situ* HT EBSD mapping is applied to directly observe the migration of the α/γ interfaces in a medium manganese steel during slow CPPTs. The behavior of (segments of) individual moving interfaces is compared with the average interface behavior of the α/γ interfaces during thermal cycling as derived from the corresponding dilatometric measurements. Furthermore, the experimental EBSD data are compared qualitatively to the results of 3D PF simulations in order to examine the effect of the actual transformation directly below the surface on which the 2D observations are made.

Experimental Details

The material selected for this *in situ* study is a hot-rolled medium Mn steel with a nominal composition of Fe-0.056C-2.0Mn (all in wt%). The same material has been used in other cyclic phase transformation studies using dilatometry and neutron depolarization, and its cyclic transformation behavior in relation to Mn partitioning has been well documented (Chen & van der Zwaag, 2016). Furthermore, for a steel of this composition, the transformation conditions can be selected such that the motion and details of the interface can be captured well given the recording time per EBSD map and the dimensions of the field of view. The low carbon concentration in this steel was selected to minimize the effect of decarburization during thermal cycling in the SEM. In this experiment, the upper and lower transformation temperatures during cycling were 1168 and 1148 K (895 and 875°C). The temperatures were selected on the basis of the preliminary EBSD observations and yielded an initial ferrite fraction at the start of the reversing heating cycle of about 80%. The microstructure of the experimental material has been investigated before and after HT observations using EBSD. At the beginning, the material contains ferritic grains with average diameter of 16.8 μm without any evidence of texture being present. The sample area (200×100 μm) observed in HT cycling, contained at room temperature 223 grains, of which 41 were edge grains.

The *in situ* EBSD experiments were conducted in a *Tescan Lyra FEG/FIB* Dual beam microscope (Brno, Czech Republic), equipped with an orientation imaging microscopy *OIM* system by EDAX including a *Hikari* Super camera (Draper, Utah, USA). Based on a trade-off between map size, spatial resolution (step size), and time resolution (framing rate) for dynamic observation of migration of phase boundaries, the EBSD images were recorded over a fixed representative area of 200 μm × 100 μm with a step-size of 1.0 μm using a hexagonal grid. Under these conditions, the recording of a single EBSD pole figure map took 50 s.

Thermal treatment inside the microscope was performed with a *Kammrath & Weiss* heating module equipped with a ceramic resistance heater (Dortmund, Germany). A thin flat sample was used, with dimensions of 10 mm × 5 mm × 0.5 mm and a finely mechanically polished surface (with 1 μm diamond paste followed by a 0.04 μm colloidal silica suspension for final polishing). The temperature was controlled via thermocouples connected to the heating element just below the specimen. The vacuum in the SEM chamber was of the order of 9×10^{-3} Pa. The EBSD detector was retracted between measurements to avoid thermal damage to the detector.

The acquisition moments for EBSD pole figure maps during the thermal cycle are shown in Figure 1, in which each point marks the collection of a new EBSD pole figure map. The same 200 μm × 100 μm region was mapped in all measurements. The imposed thermal profile is that of a type H CPPT (Chen & van der Zwaag, 2016), where the sample is held isothermally for some time at the upper and lower temperature during cycling.

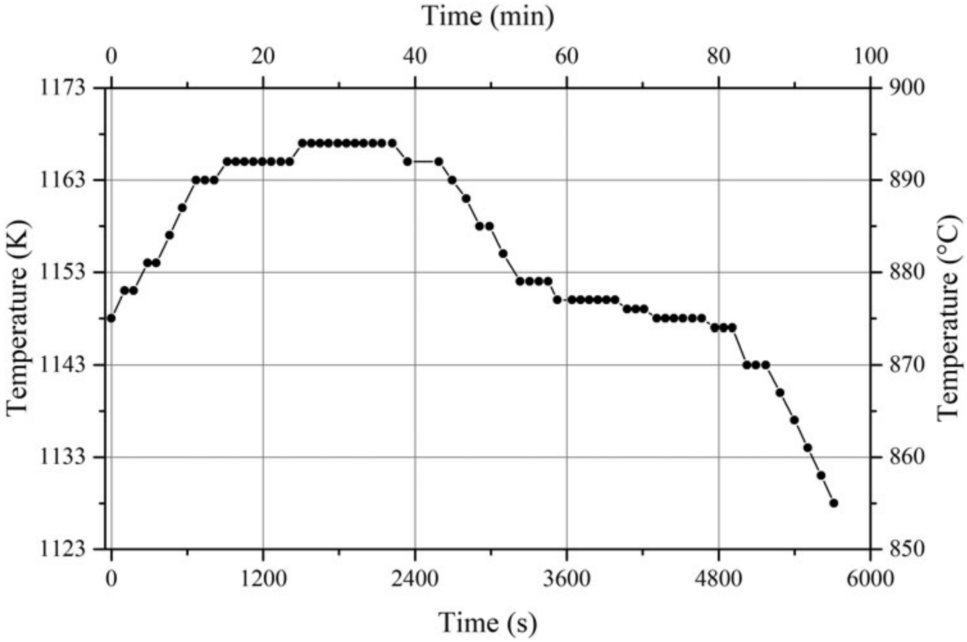

Fig. 1. Applied thermal route. Each point in the curve refers to an EBSD image recording.

Such a profile gives the best chance of measuring the direct transformation and the stagnant stages (Chen & van der Zwaag, 2016). The time $t = 0$ in Figure 1 marks the start of the reheating stage after the prior intercritical holding treatment for 3000 s.

The EBSD data were collected by means of the *TSL OIM Data Collection 7.3* software and data analysis was performed by *TSL OIM Analysis v.7.3* software (EDAX). This procedure consists of a two-step data cleaning process starting with Grain Confidence Index Standardization (setting grain tolerance angle of 5°, minimum grain size of 5 pixels at multiple rows) followed by a Neighbor Orientation Correlation procedure (level 4, tolerance 5, and a minimal Confidence Index of 0.1). After the data cleaning treatment, all data points with a Confidence Index value below 0.1 were ignored and are shown as white points in the EBSD pole figure maps. Only the second cleaning treatment step may change the orientation of the scanned points (typically <2%) but the phase allocation of each data point remained unchanged. The OR between two grains has been derived on the basis of misorientations observed between 5 and 7 pair points, all very near the phase boundary. Given the required instrument settings, the HT measurements do not allow detecting plastic deformation in the grains recorded.

Determinations of motion of the phase fronts during $\alpha \rightarrow \gamma$ and $\gamma \rightarrow \alpha$ phase transformations were done by point-wise comparison of time-sequenced EBSD phase maps, using the *Matlab* image analysis tool (The Math Works Inc., 2007). The tool identified the area swept by each interface between two successive phase maps.

Finally, in this manuscript, only one set of experiments is presented. However, based on a large number of other trial experiments, we are convinced that the findings reported here are representative for the transformation behavior in this steel as far as the transformation details can be recorded with the EBSD technique.

Phase Field Model and Simulation Conditions

The MICRESS® software (Steinbach & Pezzolla, 1999) was used to solve the PF and diffusion equations and enabled prediction of the microstructure evolution and alloy element distribution in time and space. A full 3D austenitic microstructure created by a Voronoi construction was used as the starting microstructure in the PF simulations. The calculation domain size was 45 μm × 45 μm × 45 μm.*The number of grains was adjusted to have an austenite grain size of 12 μm, i.e. the calculation domain contained 60 individual grains. The grid size employed was $\Delta x =$ 0.3 μm. Periodic boundary conditions were set for all simulations, while the analysis of the austenite/ferrite interface migration is with a focus on interfaces located in the bulk of simulation domain located far away from the domain boundaries, with mobility of the interfaces used as a fitting parameter. Crystallographic orientations were assigned to the parent austenite and newly formed ferrite grains and special misorientation boundaries with low energy and high mobility were defined (Mecozzi et al., 2005; Militzer et al., 2006). The initial 3D microstructure is shown in Figure 2, which also contains the reconstructed image for a 2D cut; the grain colors in the 2D cut represent the different crystallographic orientations. The 3D simulation results have been visualized using the *ParaView* software (Ayachit, 2015). The thermal route imposed in the simulation is time-wise identical to the one shown in Figure 1. However, different absolute temperatures were used to achieve a better fit between the PF calculations and the accompanying experimental results. More details of the thermal route and fitting parameters used in the PF simulations are presented in section “Phase Field Simulation Assisted Interpretation of the Experimental Results”.

Results of *In Situ* EBSD

In this section, the results of the HT EBSD measurements during thermal cycling are presented and discussed from various perspectives. The recorded EBSD pole figure maps are collected in Appendix A and for each map the time and temperature are reported.

In the following subsections, first, the results dealing with the overall behavior of the material are presented. Then, the behavior

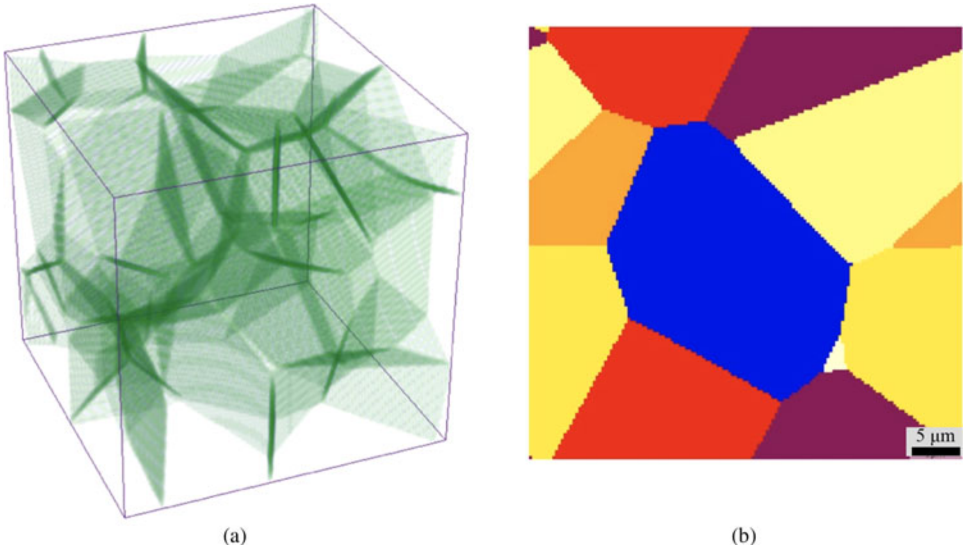

Fig. 2. (**a**) Initial austenite microstructure in 3D simulations, (**b**) 2D cut of a 3D microstructure and with different crystallographic orientations in different colors.

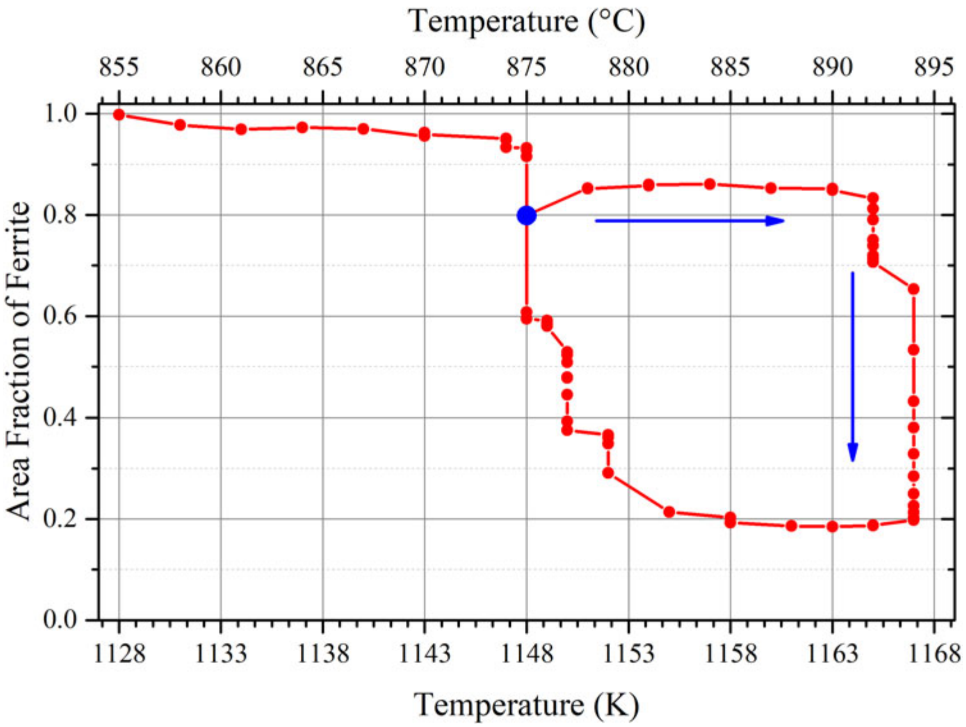

Fig. 3. EBSD measured ferrite fraction versus temperature during thermal cycling. The measurements start at the large blue data point and the curve is to be read clock-wise, as indicated by the blue arrows.

of (segments of) selected individual interphase boundaries are presented and discussed.

Overall Transformation Kinetics

The best impression of the overall transformation kinetics can be obtained by plotting the degree of transformation (i.e., the α fraction present) as a function of the temperature. Figure 3 shows the areal α fraction derived from the EBSD pole figure maps as a function of the temperature over the thermal cycle. The measurements start from the large blue data point and the curve is to be read clock-wise (as indicated by the blue arrows in the figure). Upon slow heating from 1148 to 1166 K (875 to 893°C), the ferrite fraction remains constant, notwithstanding the imposed temperature rise, reflecting the so-called stagnant stage (Chen, Kuziak, et al., 2013b; Chen & van der Zwaag, 2016). Upon further heating from 1166 to 1168 K (893 to 895°C) and holding there, a normal quasi-isothermal transformation takes place and the α fraction decreases continuously. Upon subsequent cooling, the ferrite fraction remains constant up to a

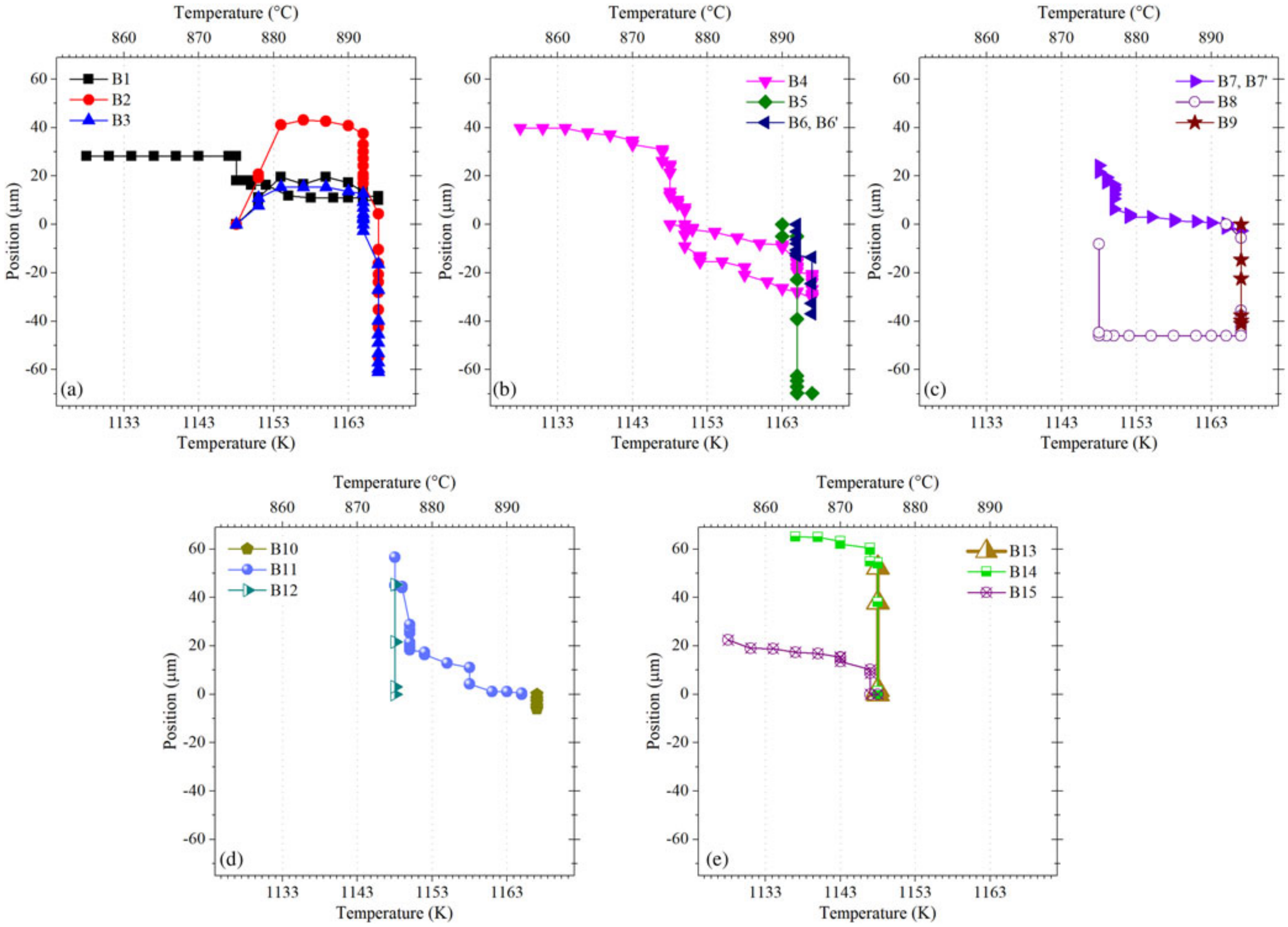

Fig. 4. Position of all 15 tracked interfaces during the cyclic transformation versus temperature of (**a**) B1, B2, B3, (**b**) B4, B5, B6, B6′, (**c**) B7, B7′, B8, B9, (**d**) B10, B11, B12, and (**e**) B13, B14, B15.

temperature of 1155 K (882°C), i.e. the sample entered another stagnant stage. Upon further cooling to 1148 K (875°C), we observe a continuous growth of the α area fraction to more or less the initial ferrite fraction. Final cooling of the sample caused the remaining γ grains to slowly disappear [the postcyclic retardation stage (Chen & van der Zwaag, 2013)], ultimately leading to a fully ferritic microstructure at 1128 K (855°C).

The overall transformation behavior during partial cyclic phase transformation as observed in EBSD is in good qualitative agreement with earlier CPPT studies using dilatometry, confocal microscopy, and neutron depolarization and shows the known distinctive stages in the process (Chen et al., 2013*a*; Chen & van der Zwaag, 2016). These stages themselves are relatively well understood and can even be reproduced in a simple 1D model which takes into account substitutional alloying element partitioning at the moving α/γ interface (Hillert, 2002).

Having established the overall validity of the EBSD experiment, it is now appropriate to turn to those rather unique features which cannot be made visible with any of the experimental techniques used so far. Hence, the next section focusses on the displacement characteristics of individual (segments of) interfaces both during the $\alpha \rightarrow \gamma$ and the $\gamma \rightarrow \alpha$ phase transformation. It should be added that the experimental conditions do not allow a reliable quantification of any grain rotation during the phase transformations, and grain rotation could have taken place unnoticed.

Local Displacement Sequences of Selected Interfaces

In this section, the displacement characteristics of 15 different α/γ interface segments are characterized in a chronological order of appearance and their migration behavior is analyzed in terms of the local crystallographic characteristics as far as they can be derived from the EBSD data. These interface segments appeared and disappeared on the sample surface at different times (and temperatures) during the thermal cycle. Figures 4a–4e show the displacement of each of the selected 15 interphases as a function of the temperature. By default, the starting position of each interface is set to zero; a positive displacement value means migration of the interface into the austenitic region (α growth), while a negative value means its migration in the ferritic region (α shrinkage), respectively. Displacement values are measured in the direction perpendicular to the local interface boundary position (as seen in the 2D measurement). Comparison of the data in Figure 3 and those in Figure 4 makes it immediately clear that the behavior of a single interface can be rather different from the overall material behavior, as derived from the time dependence of the ferrite fraction. Over the temperature range 1148–1168 K (875–895°C),

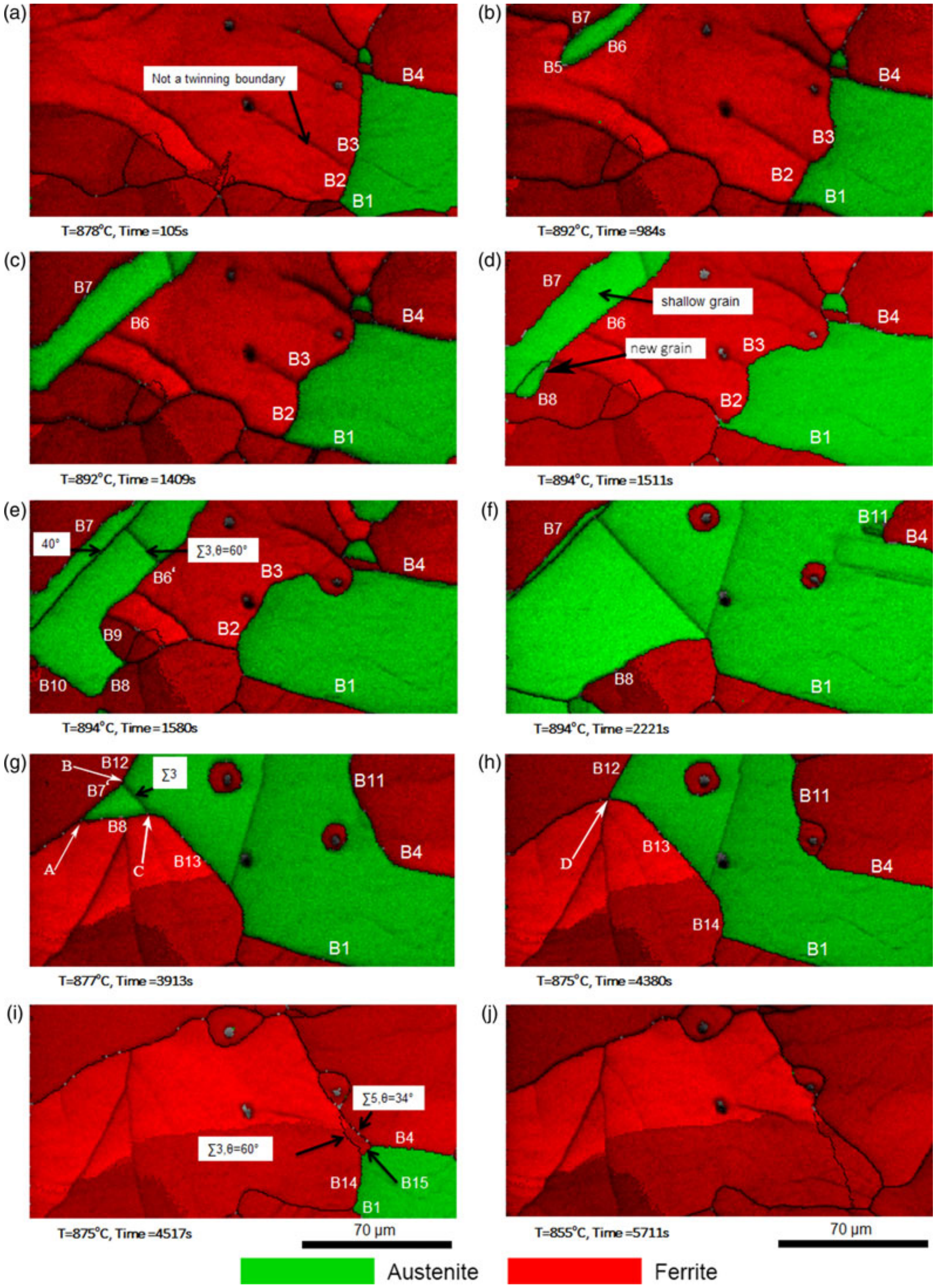

Fig. 5. Selected *in situ* EBSD phase maps showing different configurations of interphase boundaries during cyclic partial phase transformation during ferrite shrinkage (austenite growth) at (**a**) $T = 1148$ K (875°C), time = 0 s, (**b**) $T = 1151$ K (878°C), time = 105 s, (**c**) $T = 1165$ K (892°C), time = 984 s, (**d**) $T = 1165$ K (892°C), time = 1409 s, (**e**) $T = 1167$ K (894°C), time = 1511s, (**f**) $T = 1167$ K (894°C), time = 1580 s and ferrite growth at (**g**) $T = 1167$ K (894°C), time = 2221 s, (**h**) $T = 1150$ K (877°C), time = 3913 s, (**i**) $T = 1148$ K (875°C), time = 4380 s, (**j**) $T = 1148$ K (875°C), time = 4517 s, and (**k**) $T = 1128$ K (855°C), time = 5711 s.

according to Figure 3, the ferrite fraction decreases, yet some local interface displacement measurements suggest local ferrite growth (Fig. 4a) and the ferrite fraction to remain constant (Fig. 4b), but of course some interfaces also suggest ferrite shrinkage (Fig. 4b). As has also been reported by others (Offerman, 2004), the growth of the ferrite fraction does not mean that all ferrite grains grow equally and isotropically, as we assume in simple 1D models, but local competition results in interface segments growing with different speeds and sometimes even in different directions, in order to optimize the overall rate of global free energy minimization (Bos & Sietsma, 2009).

In order to analyze the migration behavior of characteristic interface segments (also contained in the video clip in the Appendix A), some EBSD images taken at successive stages of the heat treatment are selected and shown in Figures 5a–5j. Each interface segment was allocated a unique identifier for the duration

Table 1. Characters of Phase Boundaries Corresponding to Figure 5.

Transformation Stage	Phase Boundary	Average Misorientation Angle (°)	OR
Austenite growth	B1	42.9	KS (with calculated 123° inclination angle of boundary plane)
	B2	36	
	B3	37.6	
	B4	52.3	
	B5	59	
	B6	55.8	
	B6′	23.9	
	B7	42.4	KS (with calculated 170° inclination angle of boundary plane)
	B8	29	
	B9	29	
	B10	48.3	
Ferrite growth	B1	44.8	NW
	B4	52	
	B7′	35.6	
	B8	44.9	
	B11	53.7	
	B12	49.43	
	B13	56.2	
	B14	22.13	
	B15	54.2	

of its existence even though its character and growth direction may change. The behavior of these boundaries is analyzed with respect to the measured OR and phase boundary type. The character of each boundary segment grouped per subset of figures from Figure 5 is listed in Table 1. It should be noted that characterization of the interphase boundaries via the OR of the crystals at the interface determined using the 2D EBSD does not necessarily fully reflect the orientation relation in 3D. However, this characterization is useful for a first-order assessment between different interfaces when comparing their behaviors in groups.

In the following subsections, the behavior of these different interphase boundary segments during the thermal cycle is analyzed, without being able to comment on the local chemical composition at the moving interface, which, as all CPPT experiments have demonstrated, is crucial in controlling the average mobility.

Local Features Observed During Ferrite Shrinkage

Migration of Straight Interface Segments with Special OR

The interphase segments B1 and B7 are characterized as interfaces with an OR close to the Nishiyama–Wasserman (NW) and Kurdjumov–Sachs (KS) OR, respectively (Verbeken et al., 2009). Both interfaces have a limited migration during the γ growth stage (Figs. 4a, 4c). The inclination angle of the interface plane B1 and B7 with respect to the surface where the interface migration is analyzed was calculated to be equal to 123 and 170°, respectively, assuming that the interface plane is actually a closed-packed plane for both phases. During the whole thermal cycle, the OR of B1, as measured, changes between NW and KS OR, with its misorientation angle varying about 3°. Compared with the other interface segments, B1 remains almost fully pinned until final cooling to 1128 K (855°C). During the heating stage, the interface segment B7 is also very stable and barely moves. It is well accepted that mobility of an interface depends on the proximity of misorientation at the interface to a special OR (Lischewski et al., 2008). The existing OR at B1 and B7 can be held responsible for the observed low mobility during α shrinkage (γ growth).

Slow Migrating Curved Interfaces Segments with No Special OR

The B4 phase boundary segment has no special OR. This interface is quite stable and is preserved until almost the end of transformation (Figs. 5a–5j). At the start of the heating stage, while B1, B2, and B3 show slight migration toward the center of the existing γ grain, B4 remains pinned upon heating from 1148 K (875°C) to 1163 K (890°C), and then migrates directly upon further heating to 1167 K (894°C) and isothermal holding at this temperature.

The interphase boundaries B5, B6, and B7 appear more or less at the same time but migrate at different rates resulting in the formation of a γ grain with an elongated morphology. B5 and B6 are characterized as interfaces with no special OR. The calculated inclination angle of 170° at B7 means the corresponding γ grain, as indicated in Figure 5d, is so shallow and the growth of B6 can be affected by topology of the γ grain beneath the surface (Wert & Zener, 1950; Offerman et al., 2004; Fan et al., 2008; Chen & van der Zwaag, 2011).

Fast Migrating Curved Interface Segments Without Special OR

The B2 and B3 phase boundary segments have similar characteristics and are likely type $\sum 7$ interfaces (Table 1). Upon heating,

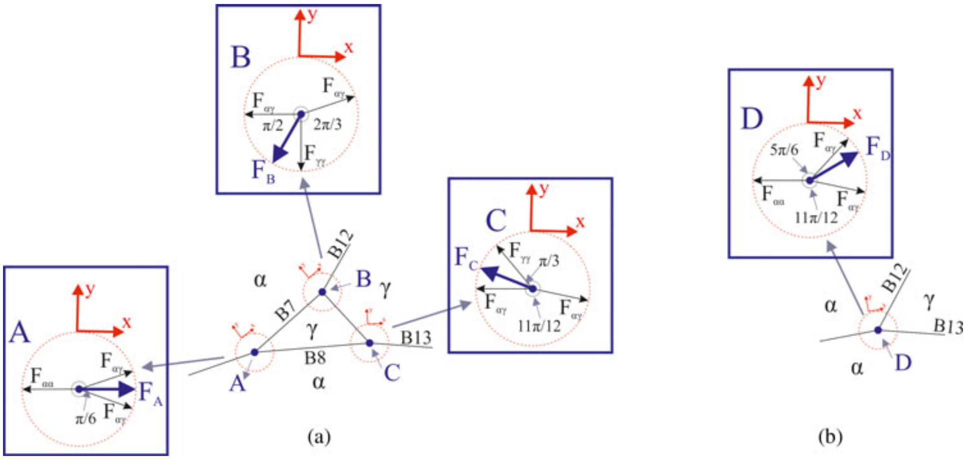

Fig. 6. Schematics of the triple junctions corresponding to configuration of interfaces and balance of interfacial tensions at (**a**) triple junctions A, B, and C and (**b**) triple junction D as shown in Figures 5g–5h.

Table 2. Summary of the Experimentally Observed Features in the Characterized Interface Segments.

Feature	Interface segments
Low velocity of interfaces with special OR	B1, B7
High velocity of interfaces without special OR	B2, B3, B8, B9, B10
Geometry effect (triple junction pinning effect)	B7′, B8 and B12, B13
Possible Mn pinning effect	B4

the semi-straight B2 and B3 α/γ phase boundaries in Figure 5b transform to the two curved interfaces in Figures 5c and 5d. During migration of these interfaces, the short area between B2 and B3 (B2/3) has a [0.69, 0.52, 0.49]@36.3° character but is no longer of the $\sum 7$ type.

The aforementioned shallow γ grain (Fig. 5d) is separated from surrounding α grains by B5, B6, and B7. Upon heating from 1165 K (892°C) to 1167 K (894°C), a new γ grain (indicated in Fig. 5e) appears adjacent to the existing shallow γ grain. By isothermal holding, the new γ grain grows relatively fast, forming new α/γ interphase segments of B6′ (appears to be a separated segment from B6 with a new misorientation angle), B8, B9, and B10. These new interphase boundary segments have no special OR and migrate rapidly, leading to considerable growth of the austenite fraction during isothermal holding at 1167 K (894°C).

Local Features Observed During α Growth

After isothermal holding, cooling starts with interphase boundaries B7 and B8 at one side and B11 and B4 at the other side of the austenite grain (Fig. 5g). The $\gamma \rightarrow \alpha$ phase transformation starts with the disappearance of the shallow γ grain, which results in a new interface segment of B7′ without any special OR and the growth of α continues with the migration of B7′ and B8.

Neighboring Fast and Slowly Migrating Interface Segments with No Special OR

The interphase boundaries of B4 and B11 are thought-provoking phase boundaries, separating the same α and γ grains from each other, but at different angles (different habit planes). As shown in Table 1, both have no special OR. As shown in Figures 5g–5j and 4b–4d, during cooling, the $\gamma \rightarrow \alpha$ phase transformation finishes early at B11 while B4 is quite stable. The stability of B4, both during heating and cooling stages (the $\alpha \rightarrow \gamma$ and $\gamma \rightarrow \alpha$ phase transformations), suggests that B4 may have been pinned by local segregation of Mn to the interface during thermal cycling.

Geometry Affected Motion of Interface Segments

The special make up of B12 and B13 interphase boundary segments during cooling (α growth) can be seen in Figures 5h–5i. As shown in Table 1, at the start of the cooling stage, both phase boundaries have no special OR. It seems that the $\gamma \rightarrow \alpha$ phase transformations at B7′, B8, B12, and B13 boundaries are interconnected: As long as B7′ and B8 exist, migration of the B12 and B13 boundaries is negligible; as soon as B7′ and B8 disappear, B12 and B13 become mobile, though their characters remain unchanged. This observation can be explained by considering the special geometrical arrangement of these interface segments. In particular, triple junctions where three or more interfaces meet are relevant in the study of interface mobility since these junctions may have the character of disclinations, i.e. the dislocation balance between the meeting boundaries is not satisfied leading to a disclination stress/strain field.

The observed behavior of B12 and B13 boundaries before and after disappearance of B7′ and B8 can be rationalized by considering the pinning effect triple junctions (Gottstein & Shvindlerman, 2006). According to the Gibbs definition of interface energy (de Gennes et al., 2004), at a constant temperature, T, and pressure, P, the interface tension of a single finite interface is related to the interface energy as

$$F_{\mathrm{k}} = \gamma_{\mathrm{k}} + A\left(\frac{\partial \gamma_{\mathrm{k}}}{\partial A}\right) + \Psi\left(\frac{\partial \gamma_{\mathrm{k}}}{\partial \Psi}\right)\left[\frac{N}{m}\right], \quad (1)$$

where F_{k} is the tension of interface k in N/m , γ_{k} is the interface energy in $\mathrm{J/m^2}$, A is the interface area, and Ψ is the misorientation angle at the interface. We assume the interface energy is independent of the interface area, $(d\gamma_{\mathrm{k}})/(dA)) = 0$. In addition, when there is no special OR at the solid–solid interface, the dependency of the interface energy to the misorientation angle is negligible, i.e. $((\partial\gamma_{\mathrm{k}})/(\partial\Psi)) = 0$. Hence, at the given condition, the interface

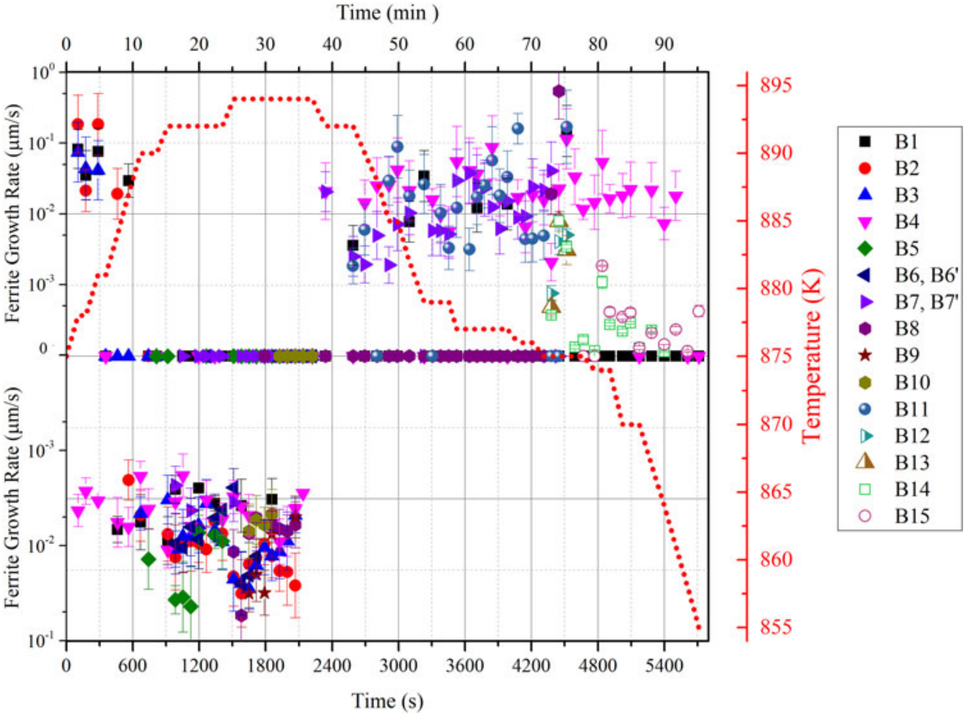

Fig. 7. Measured velocities of different boundaries and applied temperature versus time.

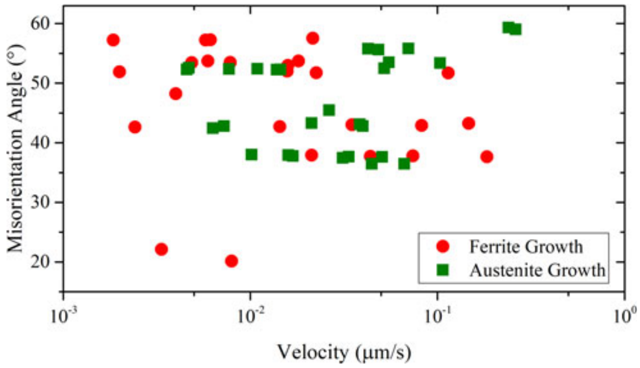

Fig. 8. Misorientation angle of interface boundaries versus their migration velocity for growth of α and γ.

energy per unit surface area can be numerically taken to be equal to the surface tension of force per unit length of the boundary.

The schematics of the A, B, C, and D triple junctions as indicated in Figures 5g–5h are sketched in Figures 6a–6b. At the moment of observation in Figures 5g–5h, no special OR is seen in at B7′, B8, B12, and B13; hence for these interfaces, the dependency of interface tension on OR in Equation (1) can be neglected. By taking interface energies of $\gamma_{\alpha\gamma} = 0.85$ J/m^2, $\gamma_{\gamma\gamma} = 0.6$ J/m^2 (Clemm & Fisher, 1955), and $\gamma_{\alpha\alpha} = 1.11$ J/m^2 (in pure Fe) (Ratanaphan et al., 2015), the equilibrium of tensions between different interfaces at the junctions for each schematic configuration of triple junctions shown in Figures 6a–6b can be calculated, assuming that the triple junction plane is orthogonal to the surface with a similar radius of curvature for all the interfaces. According to the observed angles between interfaces at the mentioned triple junctions, calculation of the absolute values of drag per unit length for each configuration leads to $F_A = 1.06$ N/m, $F_B = 0.42$ N/m, $F_C = 0.88$ N/m, and $F_D = 0.92$ N/m in the directions shown in Figure 6. These calculations confirm that the balance of tensions in the configuration of triple junctions A and D are favorable for $\gamma \rightarrow \alpha$ phase transformation, while for triple junctions B and C, the equilibrium drag force is against motion of these triple junctions toward $\gamma \rightarrow \alpha$ phase transformation. Henceforth, in conditions of availability of low chemical driving force for $\gamma \rightarrow \alpha$ phase transformation, the triple junctions A and D can accelerate the motion of B7′ and B8 interface segments in Figure 5g and B12 and B13 interface segments in Figure 5h; whereas the motion of B12 and B13 interphase boundaries adjacent to triple junctions B and C in Figure 5g seem to be *triple junction controlled* (Gottstein et al., 1999; Hilgenfeldt et al., 2004).

Final Stage of α Growth

The constitution of these phase boundaries at the final stage of cooling at 1148 K (875°C) is shown in Figure 5j. After isothermal holding at this temperature for about 205 s, migrations of B1, B4, and B14 phase boundary segments stop and these interface segments do not move further. Apart from B1, there is no special OR at B4 and B14. With further cooling to 1128 K (855°C), a new α grain appears creating the B15 phase boundary segment adjacent to B4 and B14. While B1 is pinned and migration of B4 and B14 is negligible, the $\gamma \rightarrow \alpha$ phase transformation finishes as a result of the smooth migration of B15 (Fig. 5k). The stable migration of B4 and B14 after this point can be explained by assuming compositional variations of Mn, or local enrichment of Mn in front of these interfaces existing from the previous heating cycle creating a postcyclic stagnant stage in α growth (Chen & van der Zwaag, 2013). As shown in Table 1, the misorientation angle in B15 is no different to that of B4, but the misorientation at grain boundary segments separating the α grain corresponding to B15 from its neighbors (Fig. 5j) suggests that B15 approaches

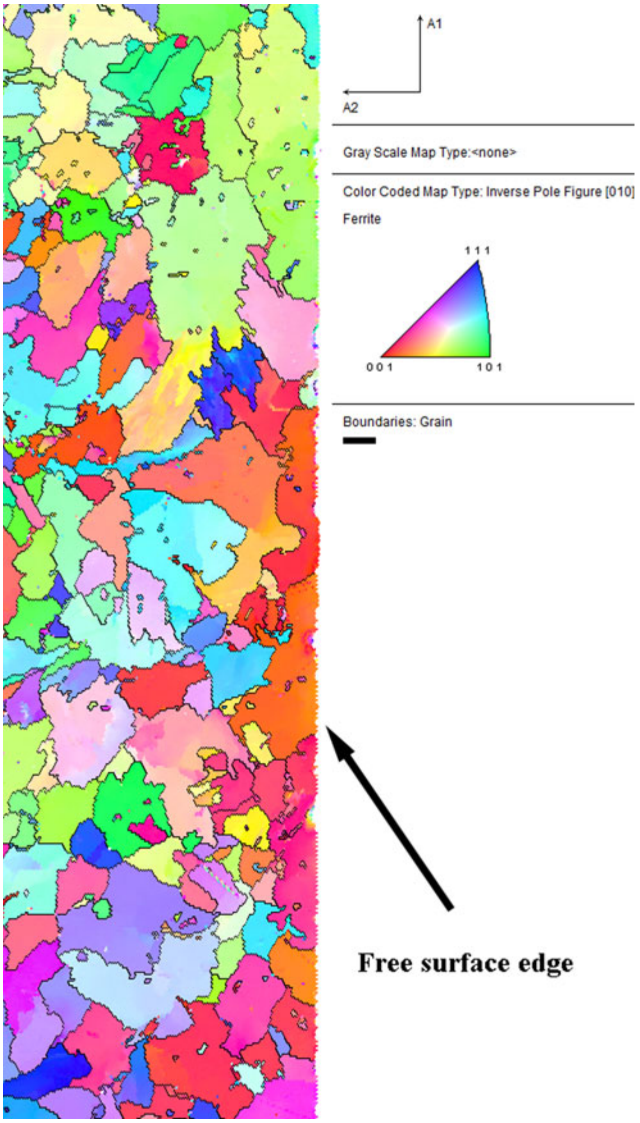

Fig. 9. The EBSD [010] Inverse Pole Figure map of the cross-section of the specimen after the high-temperature *in situ* stage.

the assumed local Mn-enriched zone from a different angle. Hence, the assumed Mn spike at B4 is ineffectual in pinning B15.

The supposed mechanisms responsible for the behavioral features of different interfaces are summarized in Table 2. The existence of special OR can be held responsible for the stagnation of B1 and B7 (during heating). Compositional variations of elements can be held responsible for the stagnation at B4 during most stages of this long treatment. Finally, the pinning effect of triple junctions can be held responsible for the behavior observed in the pair of B7′, B8 and B12, B13.

Migration Velocities of the Interfaces

The migration rate of each identified phase boundary segment can be measured from the slope of the position of interfaces versus time. The measured growth rates of the different selected interfaces and the temperature profile versus time are shown in Figure 7. The motion center of the graphs in this figure denotes zero velocity, the upper side and the lower side of the graph denotes the measured migration velocities leading to α or γ growth, respectively. The growth rates of different boundaries are widely scattered and at many points the rates drop to zero. Such a behavior is similar to the jerky motion previously reported (Yufatova et al., 1980; Zijlstra et al., 2017), however the number of boundaries studied in the present work is too limited to draw the same conclusion. The average migration rate of interface segments during the whole transformation, for both γ and α growth, can be derived from Figure 7. Comparison between average growth rates of α/γ interphase boundaries during their migrations shows no major difference between averaged growth rates of interface segments during α growth, as calculated 0.057 μm/s, and γ growth as calculated 0.080 μm/s.

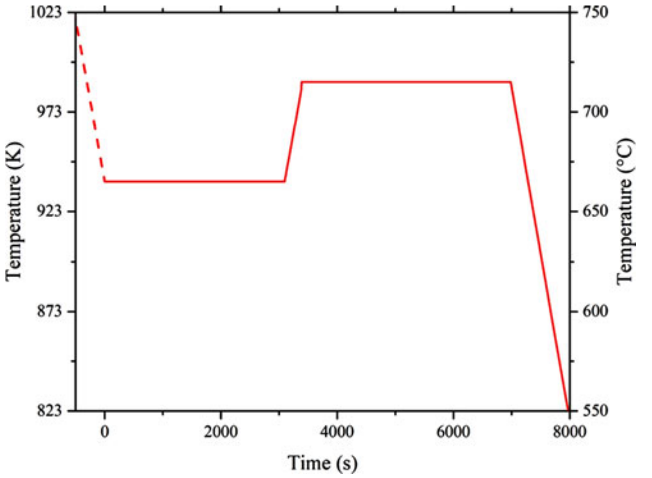

Fig. 10. The applied thermal route in the 3D phase field simulation of CPPT treatment.

A unique feature of the *in situ* EBSD measurement is the possibility to characterize and follow the misorientation angle of each identified interface segment during the cyclic treatment. Figure 8 shows the misorientation angle of some interphase boundaries versus their migration velocity during ferrite or austenite growth. Analogous to findings in Zijlstra et al. (2017), no clear correlation was found between the average migration velocity and the misorientation angle between the parent–daughter interphase boundaries.

Post transformation Analysis of the Surface

Given the long exposure time of the sample to the high intercritical annealing temperatures before and during the *in situ* experiments, in combination with the modest vacuum conditions, a cross-section of the sample perpendicular to the surface was prepared after the *in situ* experiment. EBSD analysis on this cross-section was performed to examine for anomalies due to surface decarburization, anomalous grain growth, etc. Figure 9 shows an EBSD map of the cross-section of the specimen at room temperature subsequent to the *in situ* HT observations. As observed, the important microstructural features at the free surface, i.e. the grain size and morphology of the grains, are similar to those well below the sample surface studied, which suggests that the observations on the free surface are more or less representative for those in the bulk. While the bias is not very strong, the cross-sectional cut suggests that a slightly higher than expected number of grain boundaries intersect the original observation surface

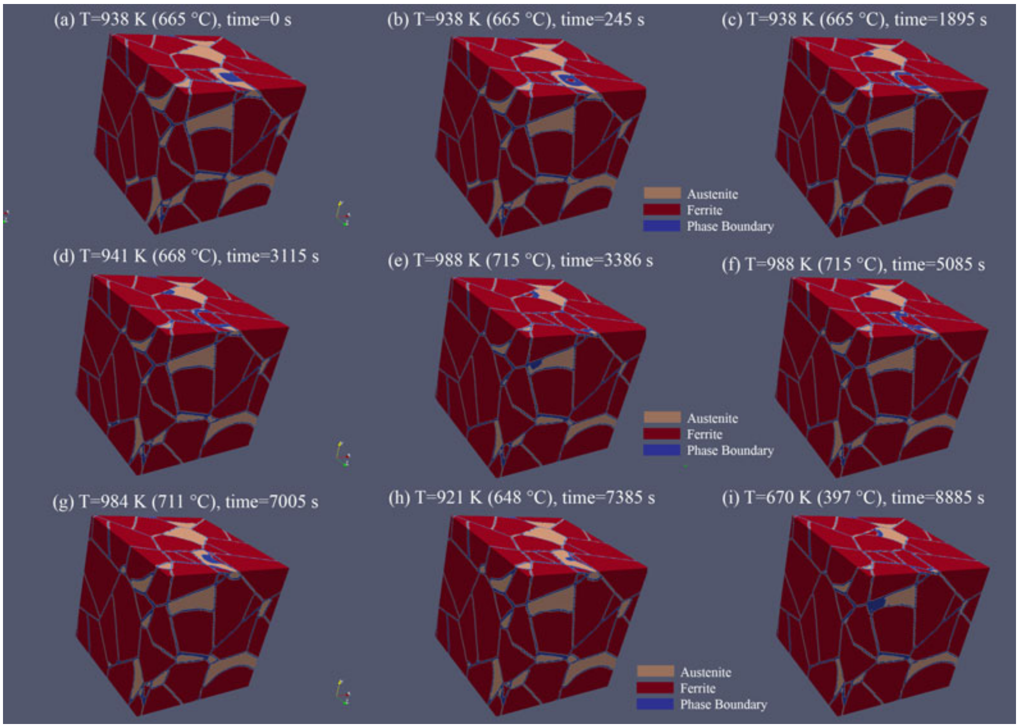

Fig. 11. Overall behavior of 3D material under simulation of CPPT treatment at different time/temperatures.

perpendicularly. This would imply that, certainly at later stages of the experiment, the EBSD observations are not too strongly affected by moving interphases intersecting the plane of observation at a shallow angle.

Phase Field Simulation Assisted Interpretation of the Experimental Results

As described in the previous section, the highly diverse local behavior observed at different interface segments can be linked to different mechanisms including compositional variations across the interface, the OR at the interfaces as well as topology and geometry effect caused by the 2D surface cut.

The thermal route imposed in the PF simulations is a typical type H route (shown in Fig. 10) and starts with cooling an austenitic microstructure from T3 (1023 K), isothermal holding of the α/γ microstructure at T1 (938 K) for 20 min, heating to T2 (988 K) and isothermal holding at this temperature for 20 min and a final cooling stage with a rate of 0.17 K/s (10 K/min). In order to avoid the effect of nucleation on the assessment, the analysis of the simulation results starts from the isothermal holding at T1, and the first cooling stage is shown with the dotted line in Figure 10. It is important to note that since the aim of using 3D PF simulation is to qualitatively investigate the effect of a 2D cut surface on the observation of behavior of interfaces during partial $\gamma \to \alpha$ and $\alpha \to \gamma$ phase transformations, no quantitative consistency between the numeric details of the simulation condition and results of the experimental observations are targeted. In this regard, to achieve the desired partial $\gamma \to \alpha$ and $\alpha \to \gamma$ phase transformation during the 3D PF simulations, the absolute temperatures of T1 and T2 were chosen to be different from those in the actual experiment.

In the next paragraphs, the characteristic behavior of the system and the displacement behavior of some selected interfaces under CPPT as calculated by 3D PF simulations are investigated.

Retraceable Back and Forth Migration of the Interfaces

The 3D video of migration of interfaces during the simulation is presented in Appendix B. Figure 11 shows some selected 3D images of the microstructure during the simulation. These images alongside the Supplementary video in Appendix B confirm retraceable back-and-forth migration of the interfaces observed in 3D PF simulation of the partial $\gamma \to \alpha$ and $\alpha \to \gamma$ phase transformations. This retraceability phenomenon has not been observed in the current *in situ* EBSD experiments reported here, but earlier scanning laser confocal microscopy studies on a leaner steel (Chen et al., 2013a) clearly suggested that some of the interface pathways are retraceable. In a recent work by Shirazi et al. (2018) using the *in situ* EBSD technique, migration of austenite–martensite interfaces during massive reversion of austenite in a Fe-11Ni alloy has been observed as being retraceable forming grains with a so-called austenite memory phenomenon. Such a phenomenon is explained by considering conditions at interfaces under massive transformation mode.

Local Features in Displacement of Interface Segments

In the EBSD data, different α/γ interface segments were observed to show different local displacement behavior upon temperature variations. Such behavior can also be observed in the PF simulation results when following local migration of interface segments at different 2D cuts. Figures 12a–12c and 12d–12f show 2D migration behavior of two groups of selected interface segments at two different orthogonal cuts of the same 3D microstructure at different times during the conditions of overall α growth. While all the α/γ interface segments existing in the given orthogonal 2D cut no. 1 (Figs. 12a–12c) are observed to follow overall growth of α grains, only a few interface segments in cut no. 2 (Figs. 12d–12f) of the same microstructure migrate toward α

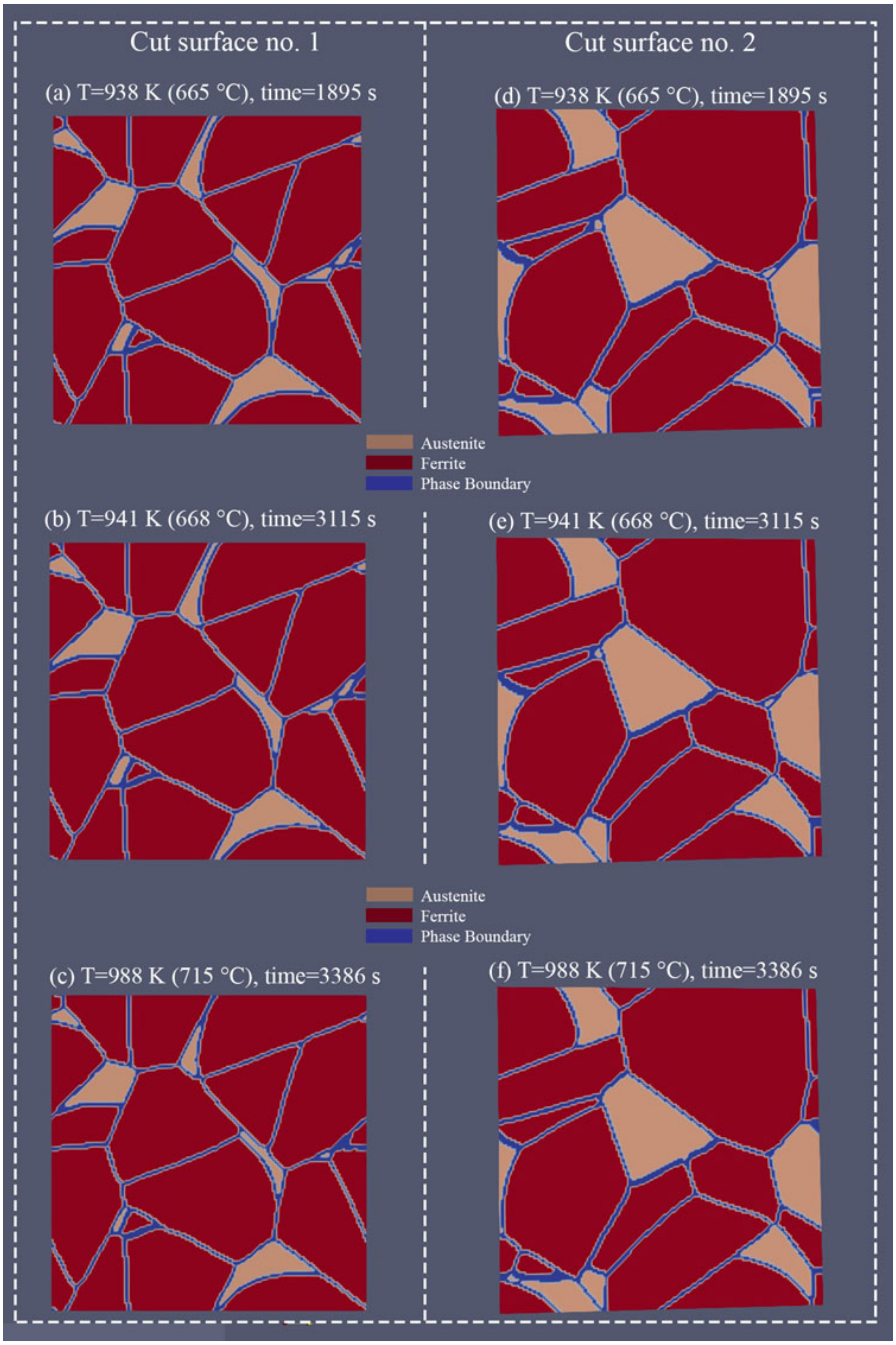

Fig. 12. Selected time/temperatures of two different 2D orthogonal cuts of the 3D simulation microstructure showing (**a**), (**b**), and (**c**) all migrating interfaces by change in temperature regime, and (**d**), (**e**), and (**f**) migration of a few interfaces and stagnation in the other existing interfaces. The videos of these two figure groups are found in Appendix C.

growth and the rest of the existing interfaces are stagnant and do not react to the change in the temperature regime. This shows that the observation of the stagnation of the present interfaces in the 2D cut of a 3D microstructure can be due to the inclination of the plane of observation, rather than to special local crystallographic or compositional conditions. The videos of these two figures are enclosed in Appendix C for further review.

Topology Effect

The effect of 3D topology of the grains on the 2D observable local features of the transformation interfaces can lead to at least three different incorrect interpretations. First, Figure 13 demonstrates how a 3D curved interface can appear as a semi-straight phase boundary segment in a 2D cut. The interface A in Figure 13a

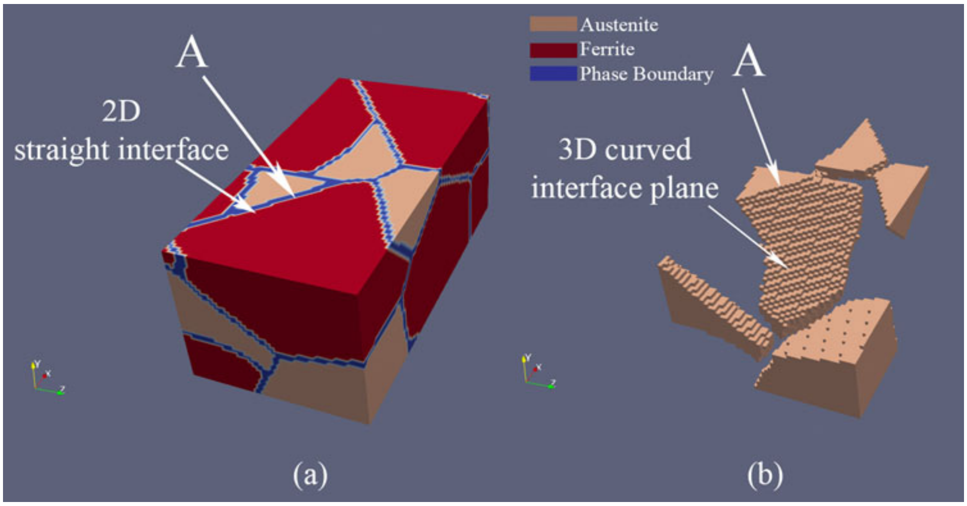

Fig. 13. Effect of topology of the grains on the apparent 2D curvature of the interfaces. **a**: An interface observed straight in 2D cut, (**b**) the same interface area observed as a 3D curved plane when removing the ferrite phase.

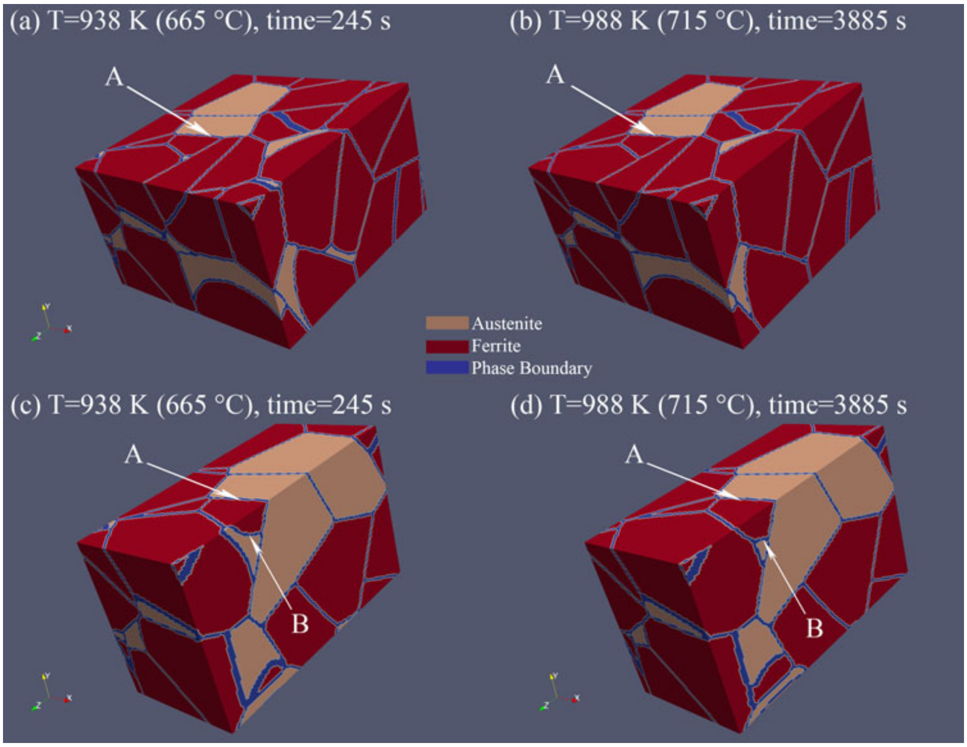

Fig. 14. Selected microstructures showing the effect of 3D topology of grains on apparent stagnation of interfaces at different time/temperatures.

appears as a straight segment in the given 2D surface cut. However, the same interface appears to be a 3D curved plane below the 2D cut surface in Figure 13b. This effect resembles the situation of the B2 and B3 interphase boundary segments that were curved around two surface defects, while the other interface segments identified in the same *in situ* EBSD maps were perceived as approximately straight lines.

The second case of misguiding 2D information concerns the 2D recorded interface velocity. In the example shown in Figures 14a–14b, the interface A as observed in the 2D cut surface appears to be immobile during the whole partial phase transformation cycle. However, when viewing the same grain from a transverse cut to that used to construct Figures 14a–14b, displacements of the interface B on the other side of the grain beneath the surface are clearly observable (Figs. 14c–14d). This confirms that the immobility of some interfaces in 2D does not necessarily mean stagnation in all of the interfaces in a particular 3D grain. This example is relevant for the correct interpretation of Figure 4, where individual interfaces are observed not to necessarily follow the overall behavior of the material which is plotted in Figure 3.

Finally, the angle between the 2D surface cut and the 3D interface plan can also have an effect on the apparent migration rate of

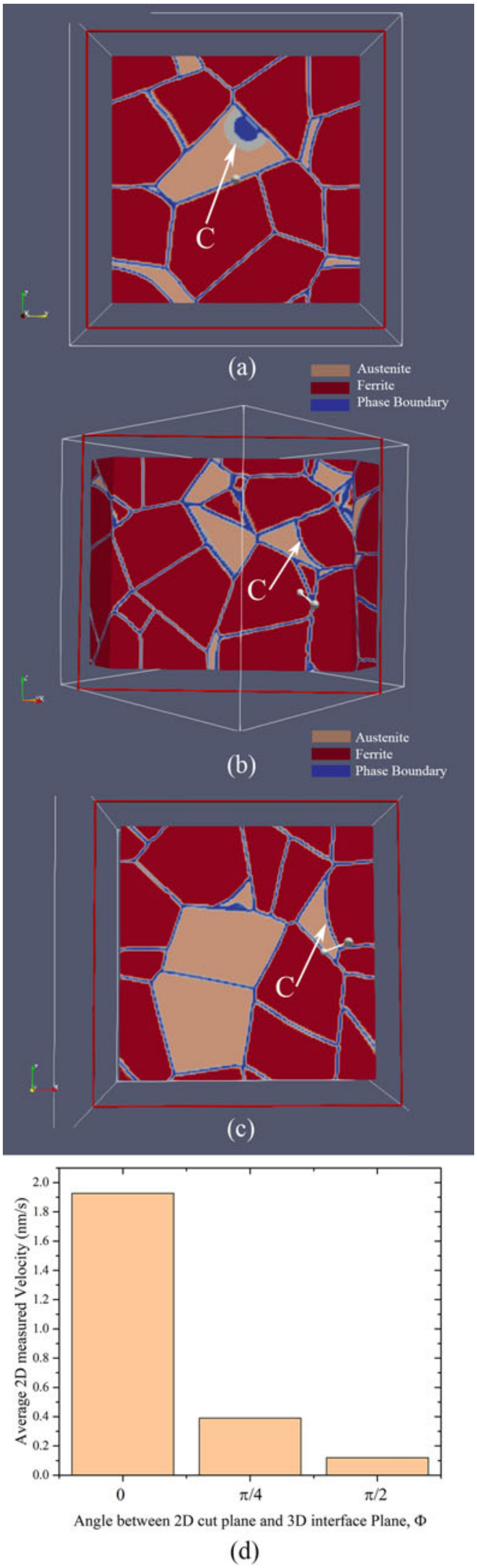

Fig. 15. The 2D cut planes showing interface C at different angles of (**a**) $\Phi = 0$, (**b**) $\Phi = \pi/4$, and (**c**) $\Phi = \pi/2$. **d:** Average measured interface C growth rate versus Φ.

the interface in 2D. Figures 15a–15c show three 2D surface cuts of interface C (as indicated in the images) at different angles of $\Phi = 0$, $\pi/4$, and $\pi/2$ corresponding to the interface plan in 3D, respectively. The average migration rate of the interface C during $\gamma \rightarrow \alpha$ phase transformation during the first isothermal holding stage measured at each of these planes is shown in Fig. 15d. The apparent velocities as measured in 2D are clearly different, while the actual velocity measured perpendicular to the interface is the same. This qualitative observation can provide a first-order explanation for the large scatter observed in the experimentally measured growth rates of different interfaces via the EBSD maps shown in Figures 7 and 8. Given the fact that at the end of the thermal cycle a large fraction of the grain boundaries appears to be more or less perpendicular to the plane of observation (Fig. 9), the effect of inclination angle may play a smaller role in the physical experiment than in the computer simulations.

Triple Junction Effect

Analysis of the *in situ* motion of the α/γ interface segments recorded via EBSD and reported in section "Results of *in situ* EBSD", shows at least one case of interphase migration to be controlled by the balance of interfacial tensions at triple junctions was observed. This situation is schematically illustrated in Figure 16a. However, no similar effect of the triple junctions was spotted in the PF simulation and the interface segments around triple junctions were observed to preserve their configuration in the back-and-forth migrations during partial $\gamma \rightarrow \alpha$ and $\alpha \rightarrow \gamma$ phase transformations, as schematically shown in Figure 16b. This difference between experimental observations and simulation results can arise from neglecting interfacial tensions around triple junctions in the simulations. As suggested in the work by Brener et al. (2009) dealing with various scenarios of dendritic melting, inclusion of this effect in future PF models could improve their accuracy in predicting microstructural evolution.

Summary and Conclusions

In this study, *in situ* HT EBSD mapping is coupled with 3D PF simulation of a comparable ferrite–austenite microstructure in combination with conditions and parameter settings leading to an equivalent change in the ferrite fraction during thermal cycling in the intercritical region. The combined results of EBSD and 2D cuts in 3D PF simulations were used to analyze the migration of the α/γ interfaces during the CPPTs in a carbon-poor medium manganese steel. The following conclusions have been reached:

1. Individual interfaces, as observed via *in situ* EBSD, do not necessarily follow the overall response of the material (characterized by area fraction of ferrite) to temperature variations.
2. The behavioral features of different interfaces can be qualitatively explained bearing in mind local conditions at the interface, i.e. crystallographic OR, topology of grains, geometrical configuration of the interfaces, and the local concentration of alloying elements around the interface.
3. Motion of the interfaces with special OR versus temperature variation was observed to be slower than that observed for interfaces without a special OR.

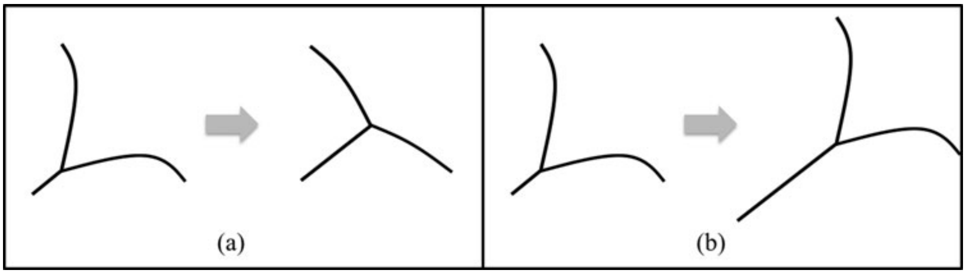

Fig. 16. Schematic representation of topology around triple junction as a result of displacement (**a**) as observed in EBSD and (**b**) as observed in the phase field simulation.

4. No relationship between OR of the interface and the likelihood of that interface showing immobility during the stagnant stage of the thermal cycle was observed.
5. No real difference was observed between average velocities of interfaces during partial $\gamma \rightarrow \alpha$ and $\alpha \rightarrow \gamma$ phase transformations. In addition, a relation between the misorientation angle and the interface velocity could not be established.
6. The range of interface velocities, as well as the scatter in velocities of individual interfaces recorded via the *in situ* EBSD maps, is found to be qualitatively explainable by the effect of 2D observation cut surface of the 3D phase transformation phenomena. The unknown angle of inclination of the moving interface with respect to the plane of observation implies that *in situ* HT EBSD measurements cannot lead to more quantitative conclusions regarding actual velocity values.
7. The α and γ grains as observed during the EBSD mapping changed shape during partial phase transformations. However, in the PF simulation, the traceable back-and-forth migration of interphase boundaries led to grain shape preservation during the imposed CPPT treatment.

Author ORCIDs. Hussein Farahani, 0000-0003-1351-7685

Acknowledgment. Hussein Farahani and Sybrand van der Zwaag gratefully acknowledge financial support of ArcelorMittal, France for their research on phase transformations in medium manganese steels.

References

Ashby M (2013). Mapping the fracture properties of engineering materials. *Philos Mag* **93**, 3878–3892. http://www.tandfonline.com/doi/abs/10.1080/14786435.2013.794983 (Accessed December 13, 2017).

Ayachit U (2015). *The ParaView Guide: A Parallel Visualization Application*. USA: Kitware, Inc.

Bos C & Sietsma J (2009). Application of the maximum driving force concept for solid-state partitioning phase transformations in multi-component systems. *Acta Mater* **57**, 136–144. https://www.sciencedirect.com/science/article/pii/S1359645408006320?via%3Dihub (Accessed July 5, 2018).

Brener EA, Boussinot G, Hüter C, Fleck M, Pilipenko D, Spatschek R & Temkin DE (2009). Pattern formation during diffusional transformations in the presence of triple junctions and elastic effects. *J Phys: Condens Matter* **21**, 464106. http://stacks.iop.org/0953-8984/21/i=46/a=464106?key=crossref.4f59cb608ef310a67e221e50e4d33f8e (Accessed July 10, 2018).

Brooks JW, Loretto MH & Smallman RE (1979). *In situ* observations of the formation of martensite in stainless steel. *Acta Metall* **27**, 1829–1838. https://www.sciencedirect.com/science/article/pii/0001616079900737 (Accessed January 4, 2019).

Chen H (2013). *Cyclic Partial Phase Transformations in Low Alloyed Steels: Modeling and Experiments*. Delft University of Technology https://repository.tudelft.nl/islandora/object/uuid:66975e4a-4b2d-4933-95c5-f180b6605882?collection=research (Accessed July 31, 2017).

Chen H, Appolaire B & van der Zwaag S (2011). Application of cyclic partial phase transformations for identifying kinetic transitions during solid-state phase transformations: Experiments and modeling. *Acta Mater* **59**, 6751–6760. http://www.sciencedirect.com/science/article/pii/S135964541100509X (Accessed March 13, 2017).

Chen H, Gamsjäger E, Schider S, Khanbareh H & van der Zwaag S (2013*a*). *In situ* observation of austenite–ferrite interface migration in a lean Mn steel during cyclic partial phase transformations. *Acta Mater* **61**, 2414–2424.

Chen H, Kuziak R & van der Zwaag S (2013*b*). Experimental evidence of the effect of alloying additions on the stagnant stage length during cyclic partial phase transformations. *Metallurgical and Materials Transactions A* **44**, 5617–5621. http://link.springer.com/10.1007/s11661-013-2040-0 (Accessed January 21, 2017).

Chen H & van der Zwaag S (2011). Modeling of soft impingement effect during solid-state partitioning phase transformations in binary alloys. *J Mater Sci* **46**, 1328–1336. http://link.springer.com/10.1007/s10853-010-4922-5 (Accessed November 4, 2016).

Chen H & van der Zwaag S (2012*a*). Indirect evidence for the existence of the Mn partitioning spike during the austenite to ferrite transformation. *Philos Mag Lett* **92**, 86–92.

Chen H & Van Der Zwaag S (2012*b*). An experimental study of the stagnant stage in bainite phase transformations starting from austenite-bainite mixtures. In *TMP 2012-–4th International Conference on Thermomechanical Processing of Steels*. Sheffield, UK, 10–12 September https://www.scopus.com/record/display.uri?eid=2-s2.0-84896891374&origin=resultslist&sort=plf-f&src=s&sid=1946a7bc694969cb3dc997da6da11cd7&sot=autdocs&sdt=autdocs&sl=18&s=AU-ID%2857188745139%29&relpos=33&citeCnt=0&searchTerm= (Accessed September 27, 2017).

Chen H & van der Zwaag S (2013). Analysis of ferrite growth retardation induced by local Mn enrichment in austenite created by prior interface passages. *Acta Mater* **61**, 1338–1349. http://www.sciencedirect.com/science/article/pii/S1359645412008051 (Accessed January 21, 2017).

Chen H & van der Zwaag S (2016). An overview of the cyclic partial austenite-ferrite transformation concept and its potential. *Metall Mater Trans A* 1–10. http://link.springer.com/10.1007/s11661-016-3826-7 (Accessed January 21, 2017).

Cheng L, Wu KM, Wan XL & Wei R (2014). In-situ observation on the growth of Widmanstätten sideplates in an Fe–C–Mn steel. *Mater Charact* **87**, 86–94. https://www.sciencedirect.com/science/article/pii/S104458031300346X (Accessed June 30, 2016).

Christian JW (2002). *The Theory of Transformations in Metals and Alloys*. Oxford: Pergamon.

Clemm P & Fisher J (1955). The influence of grain boundaries on the nucleation of secondary phases. *Acta Metall* **3**, 70–73. http://www.sciencedirect.com/science/article/pii/0001616055900146?via%3Dihub (Accessed June 30, 2016).

de Gennes P-G, Brochard-Wyart F & Quéré D (2004). *Capillarity and Wetting Phenomena*. New York, NY: Springer New York. http://link.springer.com/10.1007/978-0-387-21656-0 (Accessed May 14, 2018).

Du J, Mompiou F & Zhang W-Z (2018). In-situ TEM study of dislocation emission associated with austenite growth. *Scr Mater* **145**, 62–66. https://www.sciencedirect.com/science/article/pii/S1359646217306000?via%3Dihub (Accessed December 13, 2017).

Ecob RC & Ralph B (1981). A model of the equilibrium structure of F.C.C./B.C.C. interfaces. *Acta Metall* **29**, 1037–1046. https://www.sciencedirect.com/science/article/pii/0001616081900559?via%3Dihub (Accessed December 13, 2017).

Edmonds V & Honeycombe RWK (1978). Photoemission electron microscopy of growth of grain boundary ferrite allotriomorphs in chromium steel. *Met Sci* **12**, 399–405. http://www.tandfonline.com/doi/full/10.1179/030634578790434016 (Accessed January 4, 2019).

Enomoto M & Wan XL (2017). *In situ* observation of austenite growth during continuous heating in very-low-carbon Fe-Mn and Ni alloys. *Metall Mater Trans A* **48**, 1572–1580. http://link.springer.com/10.1007/s11661-017-3961-9 (Accessed March 15, 2017).

Fan K, Liu F, Liu XN, Zhang YX, Yang GC & Zhou YH (2008). Modeling of isothermal solid-state precipitation using an analytical treatment of soft impingement. *Acta Mater* **56**, 4309–4318. https://www.sciencedirect.com/science/article/pii/S1359645408003364?via%3Dihub (Accessed February 27, 2018).

Fukino T & Tsurekawa S (2008). In-situ SEM/EBSD observation of α/γ phase transformation in Fe-Ni alloy. *Mater Trans* **49**, 2770–2775. https://www.jstage.jst.go.jp/article/matertrans/49/12/49_MAW200824/_article (Accessed December 12, 2017).

Fukino T, Tsurekawa S & Morizono Y (2011). In-situ scanning electron microscopy/electron backscattered diffraction observation of microstructural evolution during $\alpha \rightarrow \gamma$ phase transformation in deformed Fe-Ni alloy. *Metall Mater Trans A* **42**, 587–593. http://link.springer.com/10.1007/s11661-010-0285-4 (Accessed December 12, 2017).

Gamsjäger E & Rettenmayr M (2015). The kinetics of diffusive phase transformations in the light of trans-interface diffusion. *Philos Mag* **95**, 2851–2865. http://www.tandfonline.com/doi/full/10.1080/14786435.2015.1078514 (Accessed December 13, 2017).

Gottstein G (2004). Solid state phase transformations. In *Physical Foundations of Materials Science*, pp. 389–422. Berlin, Heidelberg: Springer Berlin Heidelberg http://www.springerlink.com/index/10.1007/978-3-662-09291-0_10 (Accessed November 4, 2016).

Gottstein G & Shvindlerman LS (2006). Grain boundary junction engineering. *Scr Mater* **54**, 1065–1070. https://www.sciencedirect.com/science/article/pii/S1359646205008080?via%3Dihub (Accessed November 30, 2017).

Gottstein G, Sursaeva V & Shvindlerman LS (1999). The effect of triple junctions on grain boundary motion and grain microstructure evolution. *Interface Sci* **7**, 273–283. http://link.springer.com/10.1023/A:1008721426104 (Accessed December 12, 2017).

Gouné M, Danoix F, Ågren J, Bréchet Y, Hutchinson CR, Militzer M, Purdy G, van der Zwaag S & Zurob H (2015). Overview of the current issues in austenite to ferrite transformation and the role of migrating interfaces therein for low alloyed steels. *Mater Sci Eng R Rep* **92**, 1–38.

Gourgues-Lorenzon AF (2007). Application of electron backscatter diffraction to the study of phase transformations. *Int Mater Rev* **52**, 65–128. http://www.tandfonline.com/doi/full/10.1179/174328007X160254 (Accessed December 12, 2017).

Gourgues-Lorenzon AF (2009). Application of electron backscatter diffraction to the study of phase transformations: Present and possible future. *J Microsc* **233**, 460–473. http://doi.wiley.com/10.1111/j.1365-2818.2009.03130.x (Accessed December 12, 2017).

Guan D, Nutter J, Sharp J, Gao J & Mark Rainforth W (2017). Direct observation of precipitation along twin boundaries and dissolution in a magnesium alloy annealing at high temperature. *Scr Mater* **138**, 39–43. https://www.sciencedirect.com/science/article/pii/S1359646217302592?via%3Dihub (Accessed December 12, 2017).

Hilgenfeldt S, Kraynik AM, Reinelt DA & Sullivan JM (2004). The structure of foam cells: Isotropic plateau polyhedra. *Europhys Lett* (*EPL*) **67**, 484–490. http://stacks.iop.org/0295-5075/67/i=3/a=484?key=crossref.c67458f0b38b15f8cb6701473f7a176a (Accessed November 30, 2017).

Hillert M (2002). Nature of local equilibrium at the interface in the growth of ferrite from alloyed austenite. *Scr Mater* **46**, 447–453. http://linkinghub.elsevier.com/retrieve/pii/S135964620101257X (Accessed November 4, 2016).

Kobler A, Hahn H & Kübel C (2012). In-situ straining analysis by TEM orientation mapping (EBSD-like TEM) - direct imaging of deformation processes in nanocrystalline metals. *Microsc Microanal* **18**, 724–725.

Kostorz G (ed.) (2001). *Phase Transformations in Materials*. Weinheim, FRG: Wiley-VCH Verlag GmbH & Co. KGaA http://doi.wiley.com/10.1002/352760264X (Accessed November 4, 2016).

Lischewski I, Kirch DM, Ziemons A & Gottstein G (2008). Investigation of the $\alpha{-}\gamma{-}\alpha$ phase transformation in steel: High-temperature *In situ* EBSD measurements. *Texture Stress Microstr* **2008**, 1–7. http://www.hindawi.com/archive/2008/294508/ (Accessed December 12, 2017).

Liu J, Chen C, Feng Q, Fang X, Wang H, Liu F, Lu J & Raabe D (2017). Dislocation activities at the martensite phase transformation interface in metastable austenitic stainless steel: An in-situ TEM study. *Mater Sci Eng A* **703**, 236–243. https://www.sciencedirect.com/science/article/pii/S0921509317308833?via%3Dihub (Accessed July 9, 2018).

Mecozzi MG, Sietsma J & Van Der Zwaag S (2005). Phase field modelling of the interfacial condition at the moving interphase during the $\gamma \rightarrow \alpha$ transformation in C-Mn steels. *Comput Mater Sci* **34**, 290–297.

Middleton CJ & Edmonds DV (1977). The application of photoemission electron microscopy to the study of diffusional phase transformations in steels. *Metallography* **10**, 55–87. https://www.sciencedirect.com/science/article/pii/002608007790043X (Accessed January 4, 2019).

Middleton CJ & Form GW (1975). Direct observation of an austenite memory effect in low-alloy steels. *Met Sci* **9**, 521–528. http://www.tandfonline.com/doi/full/10.1179/030634575790444810 (Accessed January 4, 2019).

Militzer M, Hoyt JJ, Provatas N, Rottler J, Sinclair CW & Zurob HS (2014). Multiscale modeling of phase transformations in steels. *JOM* **66**, 740–746. http://link.springer.com/10.1007/s11837-014-0919-x (Accessed December 13, 2017).

Militzer M, Mecozzi MG, Sietsma J & van der Zwaag S (2006). Three-dimensional phase field modelling of the austenite-to-ferrite transformation. *Acta Mater* **54**, 3961–3972.

Mishra RK (2012). Tutorial: A guide to EBSD for in-situ studies. *Microsc Microanal* **18**, 1966–1967.

Mishra RK. & Kubic Jr. R (2008). *In situ* EBSD of microstructure evolution during deformation. *Microsc Microanal* **14**, 552–553.

Moine P, Rivieri JP, Ruault MO, Chaumont J, Pelton A & Sinclair R (1985). *In situ* TEM study of martensitic NiTi amorphization by Ni ion implantation. *Nucl Instrum Methods Phys Res Sect B* **7–8**, 20–25. https://www.sciencedirect.com/science/article/pii/0168583X85905233 (Accessed January 4, 2019).

Mompiou F, Wu J & Zhang W-Z (2015). A preliminary in-situ TEM study of martensite/austenite interface migration in an Fe-20Ni-5.4Mn alloy. *Mater Today: Proc* **2**, S651–S654. https://www.sciencedirect.com/science/article/pii/S2214785315006136?via%3Dihub (Accessed December 13, 2017).

Nowell MM, Wright SI & Carpenter JO (2009). In-situ orientation imaging of recrystallization and grain growth in OFHC copper. *Microsc Microanal* **15**, 678.

Offerman SE, van Dijk NH, Sietsma J, Lauridsen EM, Margulies L, Grigull S, Poulsen HF & van der Zwaag S (2004). Solid-state phase transformations involving solute partitioning: Modeling and measuring on the level of individual grains. *Acta Mater* **52**, 4757–4766. https://www.sciencedirect.com/science/article/pii/S1359645404003660?via%3Dihub (Accessed February 27, 2018).

Offerman SEE (2004). Microstructures in 4D. *Science* **305**, 190–191.

Onink M, Tichelaar FD, Brakman CM, Mittemeijer EJ & van der Zwaag S (1995). An *in situ* hot stage transmission electron microscopy study of the decomposition of Fe-C austenites. *J Mater Sci* **30**, 6223–6234. http://link.springer.com/10.1007/BF00369670 (Accessed December 12, 2017).

Phelan D, Stanford N & Dippenaar R. (2005). *In situ* observations of Widmanstätten ferrite formation in a low-carbon steel. *Mater Sci Eng A* **407**, 127–134. https://www.sciencedirect.com/science/article/pii/S0921509305007148?via%3Dihub (Accessed December 13, 2017).

Prior D, Seward G, Bestmann M, Piazolo S & Wheeler J (2003). EBSD at high temperatures in metals and minerals. *Microsc Microanal* **9**, 78–79.

Purdy G, Ågren J, Borgenstam A, Bréchet Y, Enomoto M, Furuhara T, Gamsjager E, Gouné M, Hillert M, Hutchinson C, Militzer M & Zurob H (2011). ALEMI: A ten-year history of discussions of alloying-element interactions with migrating interfaces. *Metall Mater Trans A* **42**, 3703–3718. http://link.springer.com/10.1007/s11661-011-0766-0 (Accessed September 26, 2017).

Purdy GR (1978*a*). The dynamics of transformation interfaces in steels-I. The ferrite-austenite interface in Fe-C-Mo alloys. *Acta Metall* **26**, 477–486. http://linkinghub.elsevier.com/retrieve/pii/0001616078901736 (Accessed July 1, 2016).

Purdy GR (1978*b*). The dynamics of transformation interfaces in steels-II. Transformations in FE-C-MO alloys at intermediate temperatures. *Acta Metall* **26**, 487–498. http://linkinghub.elsevier.com/retrieve/pii/0001616078901748 (Accessed July 1, 2016).

Raghavan V & Cohen M (1975). Solid-State phase transformations. In *Changes of State*, pp. 67–127. Boston, MA: Springer US http://link.springer.com/10.1007/978-1-4757-1120-2_2 (Accessed November 4, 2016).

Ratanaphan S, Olmsted DL, Bulatov VV, Holm EA, Rollett AD & Rohrer GS (2015). Grain boundary energies in body-centered cubic metals. *Acta Mater* **88**, 346–354. https://ac.els-cdn.com/S1359645415000828/1-s2.0-S1359645415000828-main.pdf?_tid=72bc3922-d066-11e7-86f6-00000aab0f01&acdnat=1511452597_a3c45db47ee96c655522daff572d0cf1 (Accessed November 23, 2017).

Sainis S, Farahani H, Gamsjäger E & van der Zwaag S (2018). An in-situ LSCM study on bainite formation in a Fe-0.2C-1.5Mn-2.0Cr alloy. *Metals (Basel)* **8**, 498. http://www.mdpi.com/2075-4701/8/7/498 (Accessed July 10, 2018).

Seward GGE, Prior DJ, Wheeler J, Celotto S, Halliday DJM, Paden RS & Tye MR (2006). High-temperature electron backscatter diffraction and scanning electron microscopy imaging techniques: In-situ investigations of dynamic processes. *Scanning* **24**, 232–240. http://doi.wiley.com/10.1002/sca.4950240503 (Accessed December 12, 2017).

Shirazi H, Miyamoto G, Hossein Nedjad S, Chiba T, Nili Ahmadabadi M & Furuhara T (2018). Microstructure evolution during austenite reversion in Fe-Ni martensitic alloys. *Acta Mater* **144**, 269–280. https://www.sciencedirect.com/science/article/pii/S1359645417309357?via%3Dihub (Accessed August 29, 2018).

Steinbach I & Pezzolla F (1999). A generalized field method for multiphase transformations using interface fields. *Phys D, Nonlinear Phenom* **134**, 385–393. https://www.sciencedirect.com/science/article/pii/S0167278999001293?via%3Dihub (Accessed May 31, 2018).

Svoboda J, Gamsjäger E, Fischer FD, Liu Y & Kozeschnik E (2011). Diffusion processes in a migrating interface: The thick-interface model. *Acta Mater* **59**, 4775–4786. https://www.sciencedirect.com/science/article/pii/S135964541100262X (Accessed December 7, 2017).

The Math Works Inc. (2007). *MATLAB Image Processing Toolbox Realese 2015b*. Natick, MA, USA: The Math Works Inc. https://www.mathworks.com/products/image.html

Torres EA & Ramírez AJ (2011). *In situ* scanning electron microscopy. *Sci Technol Weld Joining* **16**, 68–78. https://doi.org/10.1179/136217110X12785889550028.

van der Zwaag S, Anselmino E, Miroux A & Prior DJ (2006). In-situ SEM observations of moving interfaces during recrystallisation. *Mater Sci Forum* **519–521**, 1341–1348. http://www.scientific.net/MSF.519-521.1341 (Accessed December 13, 2017).

Verbeken K, Barbé L & Raabe D (2009). Evaluation of the crystallographic orientation relationships between FCC and BCC phases in TRIP steels. *ISIJ Int* **49**, 1601–1609. http://joi.jlc.jst.go.jp/JST.JSTAGE/isijinternational/49.1601?from=CrossRef (Accessed November 20, 2017).

Watanabe T, Obara K & Tsurekawa S (2004). In-situ observations on interphase boundary migration and grain growth during α/γ phase transformation in iron alloys. *Mater Sci Forum* **467–470**, 819–824. http://www.scientific.net/MSF.467-470.819 (Accessed December 12, 2017).

Wert C & Zener C (1950). Interference of growing spherical precipitate particles. *J Appl Phys* **21**, 5–8. http://aip.scitation.org/doi/10.1063/1.1699422 (Accessed February 27, 2018).

Witusiewicz VT, Hecht U & Rex S (2013). In-situ observation of eutectic growth in Al-based alloys by light microscopy. *J Cryst Growth* **372**, 57–64. https://www.sciencedirect.com/science/article/pii/S0022024813001656?via%3Dihub (Accessed December 13, 2017).

Witusiewicz VT, Hecht U, Rex S & Apel M (2005). *In situ* observation of microstructure evolution in low-melting Bi–In–Sn alloys by light microscopy. *Acta Mater* **53**, 3663–3669. https://www.sciencedirect.com/science/article/pii/S1359645405002417?via%3Dihub (Accessed December 13, 2017).

Wright SI, Field DP & Nowell MM (2005). Impact of local texture on recrystallization and grain growth via in-situ EBSD. *Mater Sci Forum* **495–497**, 1121–1130. https://www.scopus.com/inward/record.uri?eid=2-s2.0-33751354041&partnerID=40&md5=ace510fd8eed6cb342affa8f82e474ef.

Wright SI, Nowell MM, De Kloe R & Chan L (2014). Orientation precision of electron backscatter diffraction measurements near grain boundaries. *Microsc Microanal* **20**, 852–863.

Yufatova SM, Sindeyev YG, Gavrilyatchenko VG & Fesenko EG (1980). Different kinetic types of phase transformation in lead titanate. *Ferroelectrics* **26**, 809–812. https://doi.org/10.1080/00150198008008177

Zhang F, Ruimi A & Field DP (2016). Phase identification of dual-phase (DP980) steels by electron backscatter diffraction and nanoindentation techniques. *Microsc Microanal* **22**, 99–107.

Zhang YB, Budai JD, Tischler JZ, Liu W, Xu R, Homer ER, Godfrey A & Juul Jensen D (2017). Boundary migration in a 3D deformed microstructure inside an opaque sample. *Sci Rep* **7**, 4423. http://www.nature.com/articles/s41598-017-04087-9 (Accessed December 13, 2017).

Zhu J, Ding R, He J, Yang Z, Zhang C & Chen H (2017). A cyclic austenite reversion treatment for stabilizing austenite in the medium manganese steels. *Scr Mater* **136**, 6–10. http://www.sciencedirect.com/science/article/pii/S1359646217301732

Zijlstra G, van Daalen MMSB, Vainchtein DIDi, Ocelík V & De Hosson JtJTM (2017). Interphase boundary motion elucidated through in-situ high temperature electron back-scatter diffraction. *Mater Des* **132**, 138–147. https://ac.els-cdn.com/S0264127517306573/1-s2.0-S0264127517306573-main.pdf?_tid=815e5eaa-d03a-11e7-a556-00000aacb361&acdnat=1511433715_f40a5e9afeefcf6229b6111b79e59ead (Accessed November 23, 2017).

Appendix A: HT *In Situ* EBSD maps

Creator/Director: H. Farahani, G. Zijlstra, V. Ocelík, J. Th. M. De Hosson, S. van der Zwaag.

Description

This video shows the *in situ* high-temperature electron backscatter diffraction (EBSD) measurements during cyclic partial phase transformations in an Fe-0.056C-2.0Mn (all in mass%) alloy. The video includes the recorded EBSD pole figure maps ([001] IPF + IQ map, Phase map and IQ + GB map) and the time and temperature for each measurement. This experiment has been conducted at the Zernike Institute for Advanced Materials, University of Groningen, the Netherlands.

DOI: https://doi.org/10.4121/uuid:a390e8d4-d2dc-4f5c-9e41-03df0e5252bd

Appendix B: 3D Phase Field Simulation

Creator/Director: H. Farahani, M. G. Mecozzi, S. van der Zwaag

Description

This video shows the results of 3D phase field simulation of cyclic partial phase transformation using MICRESS software. Back-and-forth migration of austenite/ferrite interfaces during partial transformations is explicitly visible in this video. This simulation has been conducted in Delft University of Technology, the Netherlands.

DOI: https://doi.org/10.4121/uuid:327a72a5-51cd-42d5-b6b4-8b6dc6467894

Appendix C: Two Different Sections of a 3D Phase Field Simulations

Creator/Director: H. Farahani, M. G. Mecozzi, S. van der Zwaag

Description

This video shows the results of 3D phase field simulation of cyclic partial phase transformation at two different 2D sections. The interfaces show different behaviors at these two different 2D sections. This simulation has been conducted in Delft University of Technology, the Netherlands.

DOI: https://doi.org/10.4121/uuid:5bef9e0d-bb44-4186-ab70-f4c72b9b9e7a